Fourier domain optical coherence tomography system with balance detection

Adrian Bradu* **and Adrian Gh. Podoleanu**

Applied Optics Group, School of Physical Sciences, University of Kent, Canterbury, CT2 7NH, UK
**a.bradu@kent.ac.uk*

Abstract: A Fourier domain optical coherence tomography system with two spectrometers in balance detection is assembled using each an InGaAs linear camera. Conditions and adjustments of spectrometer parameters are presented to ensure anti-phase channeled spectrum modulation across the two cameras for a majority of wavelengths within the optical source spectrum. By blocking the signal to one of the spectrometers, the setup was used to compare the conditions of operation of a single camera with that of a balanced configuration. Using multiple layer samples, balanced detection technique is compared with techniques applied to conventional single camera setups, based on sequential deduction of averaged spectra collected with different on/off settings for the sample or reference beams. In terms of reducing the autocorrelation terms and fixed pattern noise, it is concluded that balance detection performs better than single camera techniques, is more tolerant to movement, exhibits longer term stability and can operate dynamically in real time. The cameras used exhibit larger saturation power than the power threshold where excess photon noise exceeds shot noise. Therefore, conditions to adjust the two cameras to reduce the noise when used in a balanced configuration are presented. It is shown that balance detection can reduce the noise in real time operation, in comparison with single camera configurations. However, simple deduction of an average spectrum in single camera configurations delivers less noise than the balance detection.

OCIS codes: (110.4500) Optical coherence tomography; (100.2980) Image enhancement; (110.4280) Noise in imaging systems; (120.3890) Medical optics instrumentation.

References and links

1. J. F. de Boer, B. Cense, B. H. Park, M. C. Pierce, G. J. Tearney, and B. E. Bouma, "Improved signal-to-noise ratio in spectral-domain compared with time-domain optical coherence tomography," Opt. Lett. **28**(21), 2067–2069 (2003).
2. R. Leitgeb, C. Hitzenberger, and A. Fercher, "Performance of Fourier domain vs. time domain optical coherence tomography," Opt. Express **11**(8), 889–894 (2003).
3. M. Wojtkowski, R. Leitgeb, A. Kowalczyk, T. Bajraszewski, and A. F. Fercher, "In vivo human retinal imaging by Fourier domain optical coherence tomography," J. Biomed. Opt. **7**(3), 457–463 (2002).
4. R. A. Leitgeb, C. K. Hitzenberger, A. F. Fercher, and T. Bajraszewski, "Phase-shifting algorithm to achieve high-speed long-depth-range probing by frequency-domain optical coherence tomography," Opt. Lett. **28**(22), 2201–2203 (2003).
5. E. Götzinger, M. Pircher, R. Leitgeb, and C. Hitzenberger, "High speed full range complex spectral domain optical coherence tomography," Opt. Express **13**(2), 583–594 (2005).
6. J. Ai and L. V. Wang, "Synchronous self-elimination of autocorrelation interference in Fourier-domain optical coherence tomography," Opt. Lett. **30**(21), 2939–2941 (2005).
7. J. Ai and L. Wang, "Spectral domain optical coherence tomography: removal of autocorrelation using an optical switch," Appl. Phys. Lett. **88**(11), 111115 (2006).
8. S. Moon, S. W. Lee, and Z. Chen, "Reference spectrum extraction and fixed-pattern noise removal in optical coherence tomography," Opt. Express **18**(24), 24395–24404 (2010).
9. A. G. Podoleanu and D. A. Jackson, "Noise analysis of a combined optical coherence tomograph and a confocal scanning ophthalmoscope," Appl. Opt. **38**(10), 2116–2127 (1999).

#167225 - $15.00 USD Received 23 Apr 2012; revised 12 Jul 2012; accepted 13 Jul 2012; published 18 Jul 2012

10. A. G. Podoleanu, "Unbalanced versus balanced operation in an optical coherence tomography system," Appl. Opt. **39**(1), 173–182 (2000).
11. I. Trifanov, P. Caldas, L. Neagu, R. Berendt, J. Salcedo, A. G. Podoleanu, and A. Ribeiro, "Combined neodymium–ytterbium-doped ASE fiber-optic Source for optical coherence tomography applications," IEEE Photon. Technol. Lett. **23**(1), 21–23 (2011).
12. C. C. Rosa and A. G. Podoleanu, "Limitation of the achievable signal-to-noise ratio in optical coherence tomography due to mismatch of the balanced receiver," Appl. Opt. **43**(25), 4802–4815 (2004).
13. Y. Chen, D. M. de Bruin, C. Kerbage, and J. F. de Boer, "Spectrally balanced detection for optical frequency domain imaging," Opt. Express **15**(25), 16390–16399 (2007).
14. D. Woods and A. Podoleanu, "Controlling the shape of Talbot bands' visibility," Opt. Express **16**(13), 9654–9670 (2008).
15. N. Nassif, B. Cense, B. Park, M. Pierce, S. Yun, B. Bouma, G. Tearney, T. Chen, and J. de Boer, "In vivo high-resolution video-rate spectral-domain optical coherence tomography of the human retina and optic nerve," Opt. Express **12**(3), 367–376 (2004).
16. N. Nassif, B. Cense, B. Hyle Park, S. H. Yun, T. C. Chen, B. E. Bouma, G. J. Tearney, and J. F. de Boer, "In vivo human retinal imaging by ultrahigh-speed spectral domain optical coherence tomography," Opt. Lett. **29**(5), 480–482 (2004).

1. Introduction

Spectral domain optical coherence tomography (SD-OCT) provides beyond doubt various attractive features over time domain optical coherence tomography (TD-OCT), such as improved signal-to-noise ratio, sensitivity and acquisition speed [1,2]. Two implementation techniques of the SD-OCT have been developed so far: Fourier domain (FD) and swept source (SS)-OCT. In terms of signal detection, FD-OCT utilizes an unbalanced detection scheme (a single spectrometer consisting amongst other components of a dispersive element such as a diffraction grating and a line camera to acquire the spectral interference fringes). In SS-OCT, as in TD-OCT, balanced detection schemes are employed. In SS-OCT, the spectral fringes at the interferometer output are sampled in time using a single point detector and a rapidly tuning narrowband source. Despite their superiority over TD-OCT, both SD-OCT implementations exhibit drawbacks in terms of autocorrelation and fixed pattern noise artifacts, which obscure details of the image and degrade the system sensitivity.

The autocorrelation terms arise from the interference occurring between different sample reflectors within the target [3]. As the amplitude of the autocorrelation terms linearly depend on the amount of light back-reflected by the sample, a simple way to eliminate them is to select a large reference reflectivity so that the autocorrelation signal is small compared to the interferometric signal. This condition is not achievable in all the applications. Another simple method to eliminate the inherent autocorrelation terms is to acquire signals from the sample arm by blocking the reference beam, store the result and then subtracting it from the interferograms. Although highly efficient, this technique is not feasible in a real time imaging system, especially when moving samples are imaged or the optical power fluctuates. Phase-shifting techniques have also been demonstrated which require several consecutive acquisitions of interferograms with precise phase-shifts implemented via piezoelectric controlled translation stages or electro-optical phase modulators placed in the reference arm of the interferometer [4,5]. Self elimination of the autocorrelation terms techniques have also been demonstrated by using: (i) a 2D CCD camera to simultaneously record both reference and sample beam spectra and then subtract them from the interferometric signal [6] or (ii) a single linear camera and an optical switch placed in the reference arm [7], where the camera records the spectra from the reference and sample arm by turning on and off the switch asynchronously.

The fixed pattern noise artifact commonly originates from the non-smoothness of the reference spectrum produced by interference. This can occur within the reference arm of the interferometer [8]. Besides, the camera themselves can exhibit an intrinsically fringed spectral responsivity while in common-path OCT systems reflective surfaces placed towards the end of the sample arm can produce significant amounts of fixed pattern noise. The optical source itself can also exhibit a fine spectral structure. Due to the fixed pattern noise artifact,

#167225 - $15.00 USD Received 23 Apr 2012; revised 12 Jul 2012; accepted 13 Jul 2012; published 18 Jul 2012

horizontal lines in the OCT images are produced. The simplest way to eliminate the fixed noise artifacts is to record the reference spectrum by blocking the sample arm and then subtract it from the interferogram. This procedure is not convenient, as during the acquisition, process fluctuations in the source spectrum can occur. An alternative to this technique is the subtraction from the interferogram not only of a single spectrum but of an averaged spectrum, obtained by acquiring a large number of consecutive spectra with the sample in place, as the averaging process will wash out the fringes of the interferometric signal. This approach is fast and efficient as long as the intensity of the reference beam is much larger than that from the sample. Furthermore, a stable light spectral intensity on the array detector is required. In SS-OCT, the fixed pattern noise artifact is canceled by the balanced detector.

Besides autocorrelation and fixed pattern noise artifacts, the OCT image quality can also be affected by the presence of the excess photon noise (EPN). This is due to random arrivals of photons from a broadband (low coherent optical source), of sufficiently large optical power. When using white light, the photon counting statistics is Bose Einstein, in which case there is EPN in top of shot noise (SN). If the optical power on the photo-detector exceeds a few microwatts, the EPN exceeds the SN and in such cases, balance detection proved useful in reducing the EPN in TD-OCT [9,10]. In SS-OCT, the photon counting statistics of the signal is closer to Poisson, which does not exhibit any EPN. In this case, balance detection is still useful in reducing the low frequency components due to power variation during the tuning.

So far, no FD-OCT with balance detection has been reported. On one hand this is justified by the fact that although white sources were employed, the saturation power of the most cameras used so far was below the level of power where EPN exceeded the SN Recently, new faster cameras (requiring larger optical powers) have been developed, with larger quantum wells, which may justify consideration of balance detection. On the other hand, there are obvious technical difficulties in balancing not a single point photo-detector, as in TD-OCT and SS-OCT, but signals delivered by an array of photo-detectors.

In this paper we evaluate a balanced detection FD-OCT system and investigate mainly, its usefulness in reducing the autocorrelation and fixed pattern noise. We also evaluate and comment on its performance in terms of excess photon noise.

2. Experimental setup

A schematic diagram of the balanced FD-OCT system implemented is shown in Fig. 1. A broadband source (BBS), based on an Ytterbium doped fiber, similar to that described in [11] (Multiwave Photonics, Porto, Portugal) with a central wavelength $\lambda = 1050$ nm and bandwidth $\Delta\lambda = 51.4$ nm was used. The optical signal originating from the BBS is divided into a reference and a sample arm by a directional coupler (DC_1, splitting ratio 80/20). In the sample arm, the beam is collimated by the microscope objective MS_1 and diverted towards the sample via the bulk beam-splitter BS (splitting ratio 50/50), the galvanometer scanning mirror GX and the microscope objective MS_2. Backscattered light from the sample is collected and guided towards a second directional coupler (DC_2, splitting ratio 50/50) where interferes with the light originating from the reference arm. In the reference arm, the distance between the microscope objectives MR_1 and MR_2 is adjustable to alter the optical path difference (OPD) in the system. Signals from the outputs of the directional coupler DC_2 are sent to two identical spectrometers. Each spectrometer consists of a microscope objective $MO_{1(2)}$, a transmission diffraction grating ($DG_{1(2)}$, 1450 lpm, Wasatch Photonics, Logan, Utah) and an InGaAs line scan camera (SU-LDH, Goodrich-SUI, Princeton, New Jersey). The SU-LDH cameras provide 14-bit digital capture, 1024 pixels (each 25x500 μm in size), a speed acquisition of up to 47,000 lines per second, a high quantum efficiency, superior to 0.85 (photo-electrons/photon) in the 1 μm region and also a full well capacity (FWC) of around 1.6 Me^-, much larger than that offered by other popular line scan cameras used in FD-OCT (for example the Aviiva EM2-EM4 cameras have a FWC of 0.3 Me^-). All the images and graphs

#167225 - $15.00 USD Received 23 Apr 2012; revised 12 Jul 2012; accepted 13 Jul 2012; published 18 Jul 2012

presented in this document where obtained with cameras acquiring data at 47,000 Hz, with the smallest possible exposure time (7 μs). For every line, a number of 512 pixels were used, while a number of 512 lines per B-scan image was employed hence an acquisition frame rate of 91.8 Hz. To ensure synchronization of data acquisition of the two cameras, an external signal generator was used to trigger each line of the two cameras and a second generator was used to trigger each B-scan image. To ensure even further synchronism between the data collected from the two cameras, the transfer of data from the cameras to computer was made via identical Camera Link cables of equal lengths and a high speed dual PCIe frame grabber (National Instruments, PCIe-1430). All quoted dB values in this manuscript are 10 times the decadic logarithm of the quantities involved.

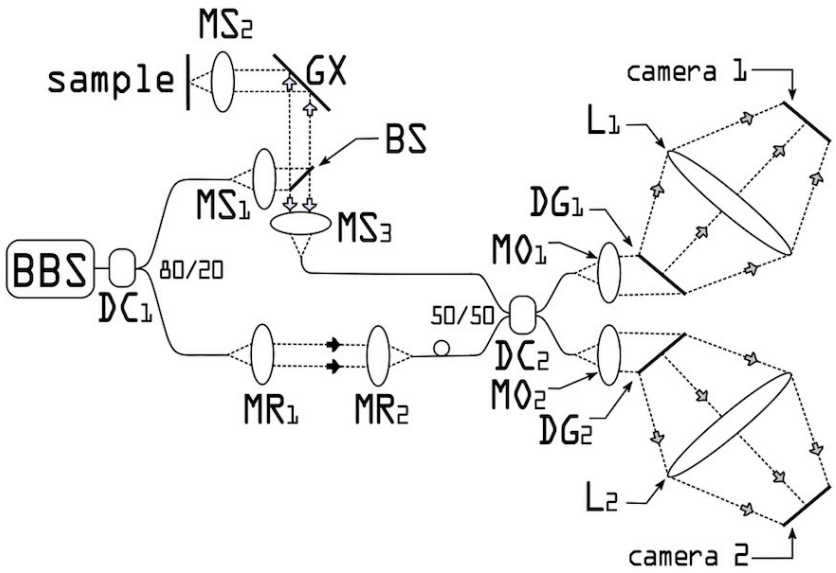

Fig. 1. Schematic diagram of the balanced FD-CT setup. BBS: broadband source; $MO_{1,2}$, MS_{1-3}, $MR_{1,2}$: microscope objectives; $L_{1,2}$: spectrometer collimators; BS: bulk beam-splitter; $DG_{1,2}$: diffraction gratings; $DC_{1,2}$: directional coupler.

3. Results

Typical optical signals measured by the two cameras are shown in Fig. 2. Although a wideband coupler has been selected (DC_2), there are still differences between the spectra in the two channels. These are due to the wavelength dependence of the splitting ratio of coupler DC_2 [12] and several other parameters in the two spectrometers that cannot be matched exactly. Supposing that the spectrometers are identical, the 50/50 coupling takes place for the central wavelength in the spectrum (around 1060 nm) with a maximum deviation of around ± 12% (i.e., 44/56 instead of 50/50) at 1030 nm. As balance detection is based on subtraction of the two signals, it is paramount to ensure that the spectra are similar as much as possible. Therefore, the two spectra have to be corrected before any subtraction. In SS-OCT, a solution to address the non-identicalness of the two spectra was reported, consisting in applying a wavelength dependent correction factor [13]. Such correction factors were calculated and after being applied to the two cameras, the noise suppression was improved by 11 dB.

A similar correction algorithm was employed for our FD-OCT implementation. The correction factor $C(\lambda)$, was calculated as the ratio between the spectrum measured by camera 1 and the spectrum measured by camera 2 which was then used to multiply the spectrum of camera 2 before being deducted from the spectrum of camera 1. After applying such correction, we observed a decrease in the noise floor level by 19.8 dB, however we cannot

#167225 - $15.00 USD Received 23 Apr 2012; revised 12 Jul 2012; accepted 13 Jul 2012; published 18 Jul 2012

claim that this improvement is due to EPN suppression but rather to a more efficient removal of the DC component.

A similar effect can be obtained in a single camera configuration where with no sample in place, from the spectrum, an average of consecutive spectra was subtracted that lead to 19.6 dB noise floor level drop. Figure 2(b) demonstrates the drop in the noise floor level for a single camera configuration obtained by subtracting an average of consecutive spectra from each interferogram. Figure 2(c) demonstrates the same level of drop, for a balanced configuration, achieved after correcting for the non-identicalness of the two spectra, using the correction factor $C(\lambda)$ obtained as described above.

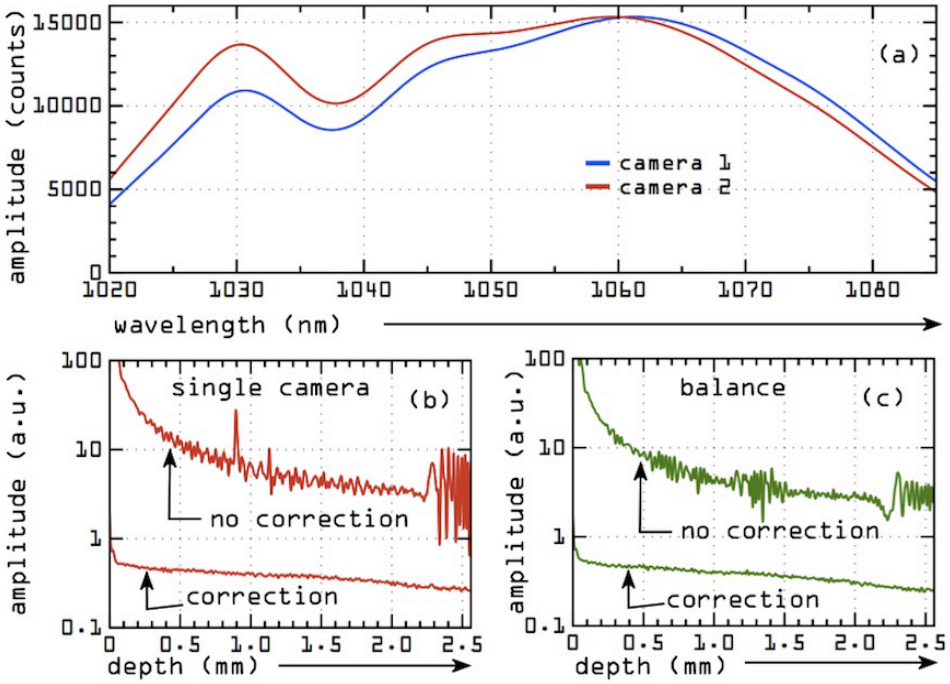

Fig. 2. (a) Typical spectra recorded by the two line cameras. (b) FFT of the interferometric signal measured by a single camera before and after correction (subtraction of an average of consecutive spectra) (c) FFT of the balanced signal before and after correction with a factor $C(\lambda)$ depending on the ratio of the two spectra (the spectra used to calculate the correction factor were obtained by averaging consecutive spectra).

Figure 3(a) shows a typical channeled spectrum recorded by the two cameras, when as sample, a flat mirror was used. The anti-phase coincidence of peaks in the two signals demonstrates nearly perfect alignment of the two spectrometers. This means that each successive pair of pixels in cameras in the two spectrometers look at similar frequency components.

The Fast Fourier Transform (FFT) of the interferograms recorded by the two individual spectrometers are shown in Fig. 3(b) (the blue and red curves) as well as the result of the balanced case (green curve), while in Fig. 3(c) the sensitivity falloff vs. depth for the three situations is shown.

#167225 - $15.00 USD Received 23 Apr 2012; revised 12 Jul 2012; accepted 13 Jul 2012; published 18 Jul 2012

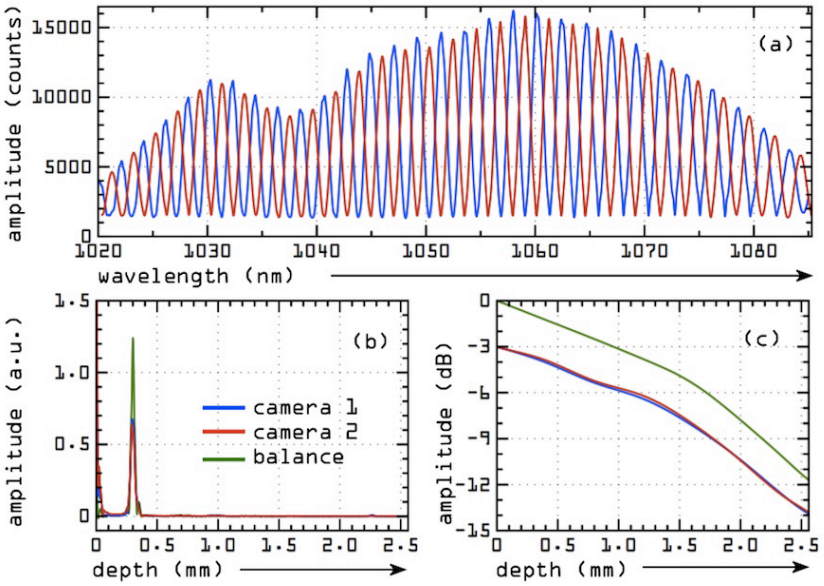

Fig. 3. (a) Interferograms recorded by the two cameras. The two signals are in anti-phase. (b) The FFT of the interferograms shown in (a) produced by each camera together with the FFT of the balanced case. (c) Sensitivity falloff across the measurement range for each of the single camera configuration and for the balance detection configuration.

3.1 Autocorrelation terms removal

To demonstrate the effectiveness of the balanced configuration on eliminating the autocorrelation terms and also of the DC components, a simple experiment was devised to produce Talbot bands [14]: as a sample, a flat mirror was used while a microscope glass slide was partially inserted into the path of the sample arm of the interferometer. As a result, three peaks can be seen in the A-scan: one due to the interference between the sample beams (one passing through the glass slide and another being delayed by it) and other two peaks due to the interference between the reference beam and the two sample beams. The peak due to the interference between the sample beams is the autocorrelation term. Figure 4 demonstrates A-scans measured by the two individual channels and by the balanced configuration.

There are three aspects that can be commented on. The first one is related to the removal of the autocorrelation terms. As the interferometric signals originating from the sample arm

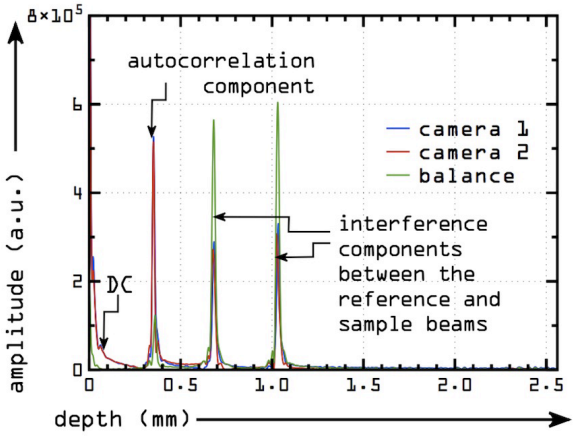

Fig. 4. Illustration of the autocorrelation terms removal.

#167225 - $15.00 USD Received 23 Apr 2012; revised 12 Jul 2012; accepted 13 Jul 2012; published 18 Jul 2012

detected by the two spectrometers are in phase, they should normally be completely extinguished by the balance configuration. In practice, a complete removal is not possible due to difficulties in obtaining perfect identical interferograms on the two cameras. Typically a reduction of the autocorrelation terms of 5-11 dB could be achieved (7 dB for the case illustrated in Fig. 4), depending on their position in depth.

The second aspect to be emphasized is the capability of the balanced detection scheme to self-eliminate the DC component without the need of any other extra measurement. Figure 4 clearly demonstrates that a balance detection scheme can remove the DC components, more efficiently than a traditional unbalanced scheme that requires an average of consecutive spectra.

Finally, the third aspect, as the interferometric signals recorded by the two cameras are in anti-phase, an enhancement of the balanced signal by 3 dB is expected. This advantage is here by a factor of 2 because the coupler DC_2 is 50/50. If from the very beginning, it is known that a single camera configuration it is to be used, then the coupler DC_2 may be adjusted to transfer 90% of power from the sample and 10% from the reference and similar interference amplitude is achievable by adjusting the attenuation in the reference path. There is some marginal advantage in the transfer of the sample signal in the balanced case, which is $2.\sqrt{0.5}$ in comparison with $\sqrt{0.9}$ in the single camera configuration, which may count when the signal is weak.

Figure 5 demonstrates B-scan OCT images obtained from an IR card in different circumstances as explained thereafter. The first two columns, (a) and (b) show images

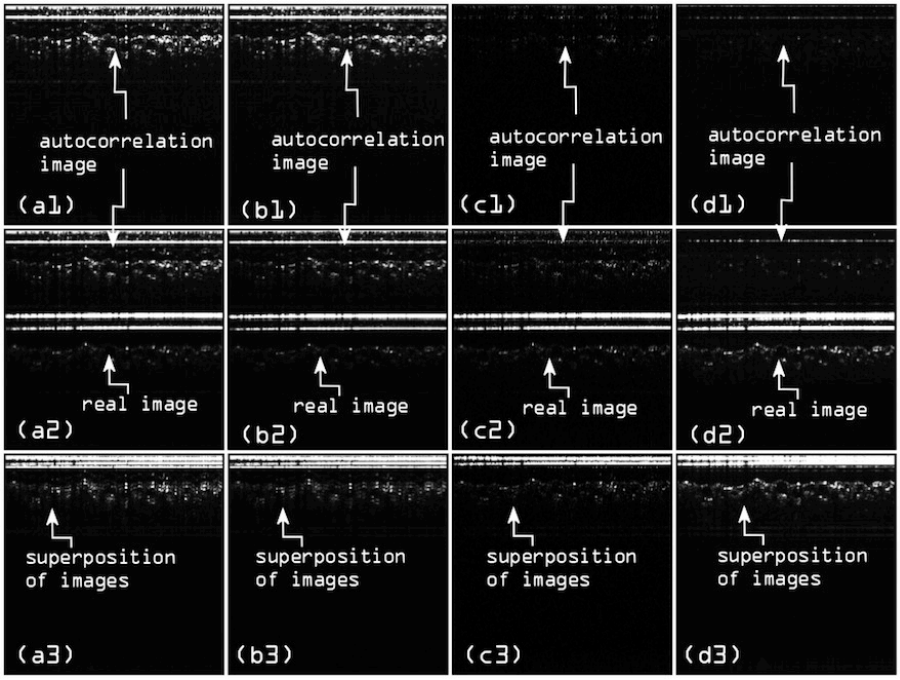

Fig. 5. B-scan images of an IR detection card demonstrating the removal of the autocorrelation image. 1st row, B-scan images collected with the reference arm blocked: 2nd row: reference arm unblocked, each frame displays at the top the autocorrelation image and underneath the image due to interference between the sample and reference beams, axially displaced to avoid their overlap; 3rd row: the autocorrelation and real image are nearly in perfect overlap; (a) column: B-scans recorded by camera 1; (b) column: B-scans recorded by camera 2; (c) column: B-scans delivered by camera 1 only, obtained by deducting an image recorded prior to measurement with the reference beam off; (d) column: B-scans delivered by the balance detection.

#167225 - $15.00 USD Received 23 Apr 2012; revised 12 Jul 2012; accepted 13 Jul 2012; published 18 Jul 2012

produced by each camera, the third column, (c), images obtained by deducting a prior image, obtained with the reference beam off and the 4th column, (d), images generated using the balance detection scheme. The images in the first row were produced with no reference power, so the features seen represent the autocorrelation images only. The second and third rows of images in Fig. 5 were acquired with both sample and reference arm unblocked. The images here contain the real interference image as well as the autocorrelation terms.

Figure 5(c1) proves that is possible to reduce the autocorrelation image substantially simply by subtracting an image of the sample previously recorded with the reference arm blocked from each image. However, such a procedure is not feasible when imaging moving samples. Even if the sample was stationary, if the optical power changed, then the autocorrelation terms will reappear. The attenuation of autocorrelation terms in the image in Fig. 5(d1), produced by balance detection, may not be as good as in Fig. 5(c1), but is performed in real time. Therefore, the balance detection will provide the same stable image irrespective of sample movement and irrespective of optical power fluctuation.

By adjusting the reference path length, actuating on the distance between MR_1 and MR_2, the real images were shifted towards larger OPD values (corresponding to larger frequencies), so the autocorrelation and the real image do not overlap at all, as seen in the second row. However, placing the sample away from OPD = 0 leads to a poor sensitivity of the image, as the sensitivity decays with OPD (and the frequency in the FFT spectrum). In case the image is brought towards OPD = 0, then it will overlap with the autocorrelation image.

Such a situation often happens in practice. For instance, in microscopy, when the sample to be imaged is placed behind a microscope glass slide, the sample features in the autocorrelation image and in the useful image overlap each other. As in the single camera scheme, the autocorrelation terms cannot be extinguished; the only possibility is to try to superpose the image created by the autocorrelation terms to the real image by actuating onto the reference path length. Doing so, images in the third row in Fig. 5 were obtained. If the overlap is imperfect, then the image resolution will suffer (Fig. 5(a3) and 5(b3) look blurry). On the other hand, the sharpness of the balanced image (Fig. 5(d3)) is completely immune to the axial position of the sample.

To quantify the suppression level of the autocorrelation terms, in Fig. 6 we plotted averaged A-scans inferred from the B-scan images presented in Figs. 5(a1), 5(b1) and 5(d1).

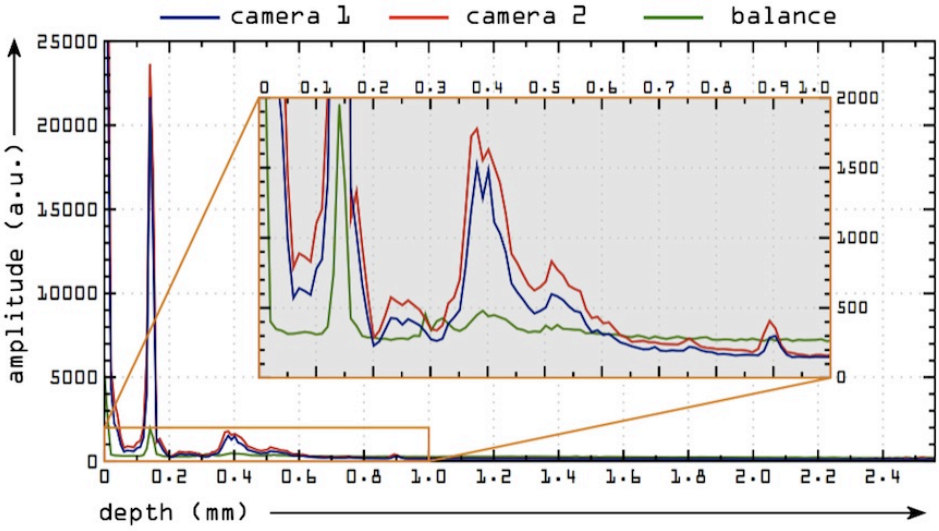

Fig. 6. Averaged A-scans inferred from the B-scan images in Figs. 5(a1), 5(b1), 5(d1). The zoomed plot demonstrates the self-elimination of the auto-correlation terms.

#167225 - $15.00 USD Received 23 Apr 2012; revised 12 Jul 2012; accepted 13 Jul 2012; published 18 Jul 2012

As commented in connection with Fig. 4 above, the balance detection self-removes the DC terms, and diminishes the autocorrelation terms: the peak at z = 0.14 mm is reduced by 10.5 dB, while the other peak at z = 0.38 mm by 5.5 dB. In connection to the noise behavior, it can be noticed that at large OPD values (above z = 0.7 mm in Fig. 6), the noise floor level of the balanced configuration is above the noise floor level of the single detection channels. This shows that the noise contributions from the two channels add up. In relation to this behavior, please see the comments in the last paragraph on *Excess photon noise*.

In Fig. 7(a) we plotted averaged A-scans inferred from the B-scan images in Figs. 5(a2), 5(b2) and 5(d2). These images contain the autocorrelation terms up to 0.95 mm followed thereafter by the useful real image of the sample (between z = 1 mm to z = 2 mm). The peak residing at around z = 1.03 mm corresponds to the top of the IR card. The next peak corresponds to a reflective specular layer in the IR card (perhaps the bottom of the protective polymer layer) at 1.13 mm. The difference of 0.1 mm gives the location of the 1st strong peak in the autocorrelation image in Fig. 7(a). Figure 7(b) shows averaged A-scans inferred from the B-scan images in Figs. 5(a3), 5(b3) and 5(d3). As the real and the autocorrelation images overlap to some extent, it is expected that the profiles generated by an unbalanced detection scheme are affected by autocorrelation. To quantify to what extent the images are affected by autocorrelation, we compare for instance the amplitudes of the peaks at around z = 1.4 mm in Fig. 7(a), not affected by autocorrelation (as they are axially away from the autocorrelation image) to the same amplitude of the peaks, in Fig. 7(b) now moved to around z = 0.4 mm, within an axial range where autocorrelation terms are present.

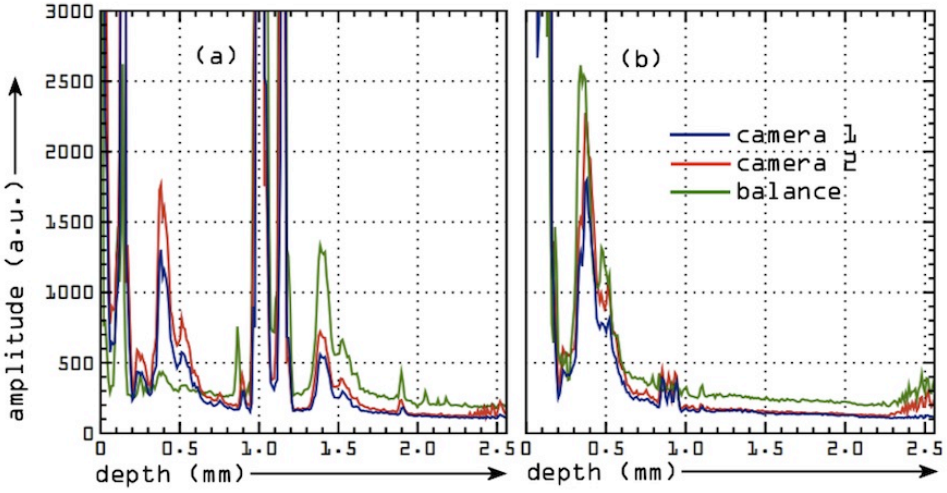

Fig. 7. (a) Averaged A-scans inferred from the B-scan images in Figs. 5(a2), 5(b2), 5(d2). (b) Averaged A-scans inferred from the B-scan images in Figs. 5(a3), 5(b3), 5(d3).

Due to sensitivity decay with OPD, the signal drops by 3 dB from z = 0.4 mm to z = 1 0.4 mm [Fig. 3(c)]. Therefore, it is expected that by moving any peak from 1.4 mm to 0.4 mm, its value should double. This happens indeed for the balance detection peak (the amplitudes of the signal peaks vary from 1300 to 2600). However, the amplitude of the peaks delivered by single cameras apparently display enhancement by more than a factor of 2, camera 1 from 550 to 1700 and camera 2, from 700 to 2300.

The self-elimination of the autocorrelation terms and of the DC components is highly dependent on the synchronism of the two cameras. Comparative averaged A-scans are shown in Fig. 8 collected for synchronized [Fig. 8(a] and free running [Fig. 8(b)] regimes. The A-scans are inferred from B-scan images in Figs. 5(a1), 5(b1), and 5(d1). These show that the noise floor level is immune to the synchronization, while the effectiveness in suppression of

#167225 - $15.00 USD Received 23 Apr 2012; revised 12 Jul 2012; accepted 13 Jul 2012; published 18 Jul 2012

the autocorrelation and DC terms in the balanced configuration depends on synchronization. The amplitude of the autocorrelation peak is reduced to 500 in comparison to 1500 in the free running mode.

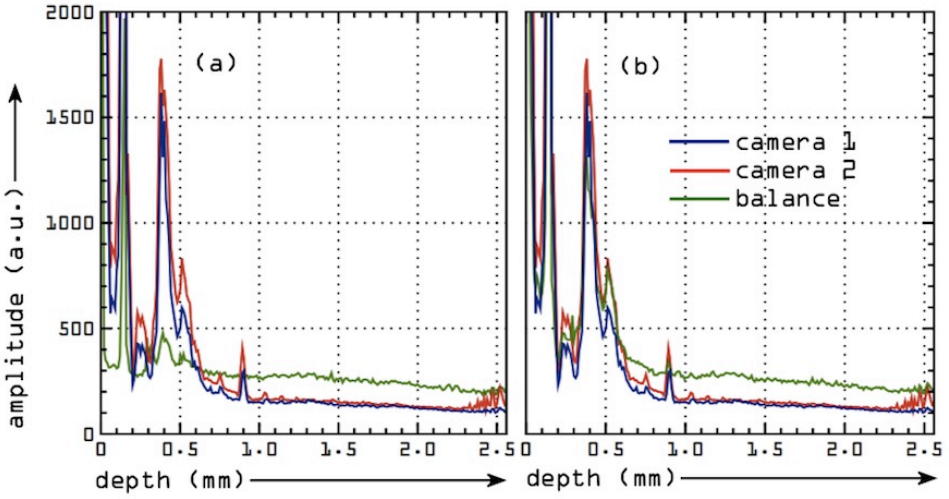

Fig. 8. Averaged A-scans over B-scan images shown in Figs. 5(a1), 5(b1), 5(d1) obtained when data acquisition by the two cameras was perfectly synchronized (a) and free running (b).

3.2 Fixed pattern noise removal

This artifact is manifested by horizontal lines (constant depth) in the B-scan images, whose intensity depend on the optical power. Figures 9(a1), 9(b1) show unprocessed images recorded by the two cameras of a tooth, exhibiting pattern noise. In Fig. 9(c1) the raw unprocessed balanced image exhibits less pattern noise than the corresponding unbalanced images in Figs. 9(a1), 9(b1). We now compare the balance detection method with two procedures for fixed pattern removal in single camera configurations.

3.3 Using priory acquired spectra with both beams on

An efficient approach to remove the fixed pattern noise in single camera configurations is to record a channeled spectrum, ACS, by averaging all channeled spectra corresponding to each A-scan in the B-scan image. This leads to a channeled spectrum, which is then deducted from each channeled spectrum, CS, of each current acquisition before FFT. Modulation of the spectrum from a transversal pixel to the next differs according to the axial structure of the sample along the depth. By averaging, the modulations due to the object structure are washed out in comparison with the modulation due to the fixed pattern noise, which survives the averaging process. The deduction of channeled spectra before FFT leads to reduction of the fixed pattern noise. Such a method has however the disadvantage that by averaging, dominant features in the object are retained and emphasized in the final ACS. For instance, if the sample is made of layers oriented exactly along the horizontal lines, then the ACS will select the modulation corresponding to the depth of that layer and will extend the layer in the final image to regions outside its transversal position in the image. The same happens for top specular surfaces of samples, when oriented horizontally.

Figures 9(a2), 9(b2) show images obtained after subtracting the ACS spectrum from the spectra, CS, acquired by each camera, followed by FFT applied to the difference of spectra: CS-ACS. As shown, large amplitude reflection from parts of the sample are extended laterally at the same depth, in the form of white stripes, while the main bright line in (a1) and (b1) is successfully removed. In Fig. 9(c2) the balance image is shown. This image was obtained by correcting for non-identicalness of the spectra by a factor $C(\lambda)$ defined as the ratio between

#167225 - $15.00 USD Received 23 Apr 2012; revised 12 Jul 2012; accepted 13 Jul 2012; published 18 Jul 2012

the ACSs recorded by the two cameras. However this does not help in removing the white stripes due to the object structure, extending laterally, due to the same deficiency of the method commented as for the single camera scheme.

3.4 Using priory acquired spectra with the sample beam off

A similar procedure consists in creating the averaged spectrum ACS with the sample beam off. This however complicates the hardware, as it requires a controllable shutter to toggle the sample beam on and off. This leads to a better removal of the fixed pattern noise, as shown in Figs. 9(a3), 9(b3). No horizontal lines due to the sample surface are seen. Similar quality of images is displayed in the balance detection image in Fig. 9(c3).

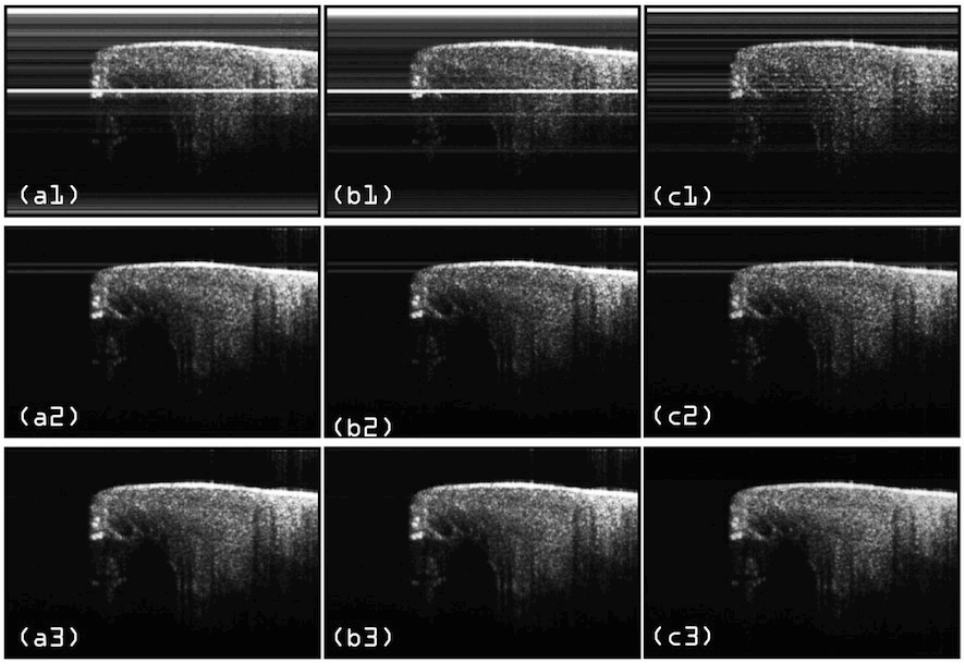

Fig. 9. B-scan images of a bovine tooth. Top row: raw images recorded (a1), (b1) by individual cameras and (c1) by the balanced scheme. Middle row (sample in place): elimination of the fixed pattern noise in images recorded by (a2), (b2) individual cameras by deducting the ACS from the spectra and (c2) in the balance case by correcting for the non-identicalness of the spectra. Bottom row, the same as middle row but with the sample arm blocked.

The two methods above are highly efficient as long as the system parameters are stable, the sample is stationary and the optical power is constant. In order to demonstrate the effect of power fluctuations on the methods above, images in Fig. 10 were acquired. To this goal, the power in the reference arm was increased by 10% for the images in the second row. Left column represents images with a single camera while the right column shows images using balance detection. Figure 10(a1) shows an image where the fixed pattern noise was eliminated by subtracting the ACS from the instantaneous spectrum photo-detected by a single camera configuration (the same image as in Fig. 9(a3). Then, in Fig. 10(a2), the pattern noise, seen as the horizontal line in Fig. 9(a1) and Fig. 9(b1), re-appears due to the change in the optical power.

The balance configuration however can be devised immune to such effect, as illustrated in the right column of images in Fig. 10. Tolerance to reference power variation is achieved by correcting the spectrum acquired by each camera with a correction factor defined as the ratio between the two ACS. Figure 10(b2) shows that even after changing the power in the

#167225 - $15.00 USD Received 23 Apr 2012; revised 12 Jul 2012; accepted 13 Jul 2012; published 18 Jul 2012

reference arm, the fixed pattern noise is still successfully canceled, as there is no trace of the horizontal line seen in Fig. 10(a2).

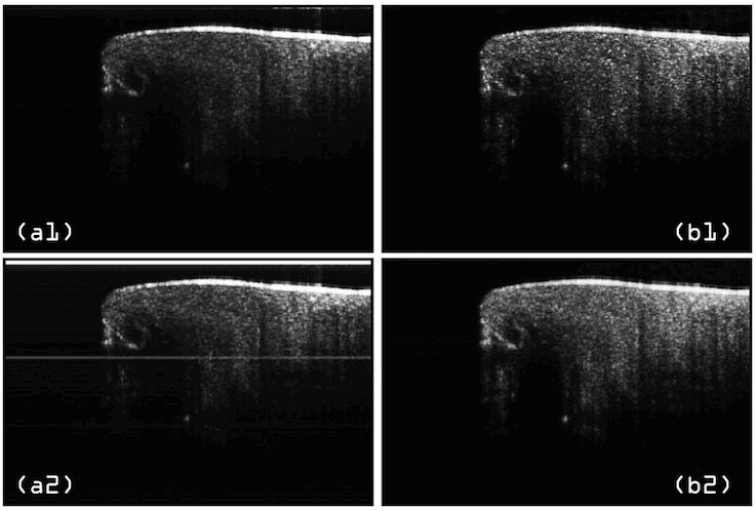

Fig. 10. B-scan images of a tooth. (a1) and (a2) images are recorded using individual cameras, (b1) and (b2) images are produced by the balance detection scheme. For the bottom row images, the optical power reaching the cameras was increased in comparison to the power used to produce the top row images, by reducing the attenuation of reference power by 10%.

3.5 Excess photon noise

First we verified that the contributions of the dark and readout noise to the overall noise are smaller than those of the shot noise and excess photon noise. For this purpose we followed the procedure described in [15]. Thus, the noise was determined by calculating the variance at each camera pixel for 1024 consecutive spectra. In Fig. 11 the noise variance at each camera pixel vs. wavelength is presented. Dark noise measurements were taken with no light on the photo-detectors (the dark curve). To measure the overall noise in the system, only light returning from the reference arm of the interferometer was used (red curve).

As shown in Fig. 11, the overall noise in the system is about 5 times larger than the dark and readout noise. When the optical power on the photo-detectors reaches about 20% of the saturation value, the SN and EPN dominate dark and readout noise.

To facilitate the calculus of the SN and EPN in our system, we express the noise in electrons squared per readout cycle and per detector element [1,16]. Mathematically we can evaluate the SN and EPN as, respectively,

$$\text{Shot noise: } \sigma_{SN}^2 = \frac{\eta e^2 P \tau_i}{E} \tag{1}$$

$$\text{Excess photon noise: } \sigma_{EPN}^2 = \left(\frac{\eta e P}{E}\right)^2 \tau_i \tau_{coh} \tag{2}$$

where η takes into account the quantum efficiencies of the spectrometer and camera, P is the optical power incident on a single detector, τ_i is the integration time of the camera, E is the energy of a single photon, $\tau coh = \sqrt{\frac{2\ln 2}{\pi}} \cdot \frac{\lambda_0^2}{\delta\lambda} \cdot \frac{1}{c}$ is the coherence time, $\delta\lambda$ being the spectral width seen by a single detector, and c is the speed of light.

#167225 - $15.00 USD Received 23 Apr 2012; revised 12 Jul 2012; accepted 13 Jul 2012; published 18 Jul 2012

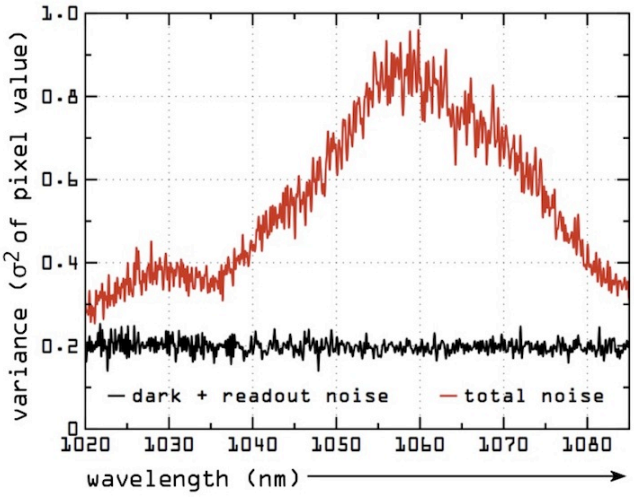

Fig. 11. Noise variance at each camera pixel for 1024 consecutive spectra. The dark and readout noise were measured with no optical power on the detector.

In our particular case, $\eta = 0.6$ (the quantum efficiency of the detector is around 0.85, the transmission coefficient of the diffraction grating is around 0.8, while around 14% of the power is lost due to the digital trimming of the spectrum), $\tau_i = 7$ μs (the camera was triggered at full speed), $\delta\lambda = 0.127$ nm (65 nm spread over 512 pixels).

To calculate the number of photons which saturates the photo-detectors, we can use the equation

$$P_{sat} = \frac{FWC}{\eta} \cdot \frac{E}{\tau_i} \tag{3}$$

As FWC = 1.6 Me^-, the camera will theoretically saturate when the power at the input of the spectrometer is 72 nW per photo-detector. On the other hand, the excess photon noise dominates the shot noise as long as the optical power per photo-detector $P \geq \frac{E}{\eta \cdot \tau_{coh}}$. In our case, to be in an excess photon noise regime, an optical power per photo-detector superior to 16.4 nW is necessary, value much lower than the saturation power of the detector. In other words, for powers between 16.4 nW and 72 nW, EPN dominates the SN.

In Fig. 12, a graphical representation of the RMS^2 versus optical power is presented, measured at the input of one of the spectrometers. Results for the single camera (red and blue) and for the balanced configuration (green) are shown. For the balanced configuration, the spectra were corrected for non-identicalness as presented in connection with Fig. 2c, before deduction. For input powers exceeding 20 μW, some pixels of the linear camera saturate. Considering a factor of 0.86 due to spectral shaping and 512 pixels, this gives an experimental saturation optical power per pixel of 33.6 nW. As shown by the red curve, the dependence is nonlinear, as proof for extra noise in top of the SN. The curve for the balance detection (middle, green) however is closer to linear, at least in the first part, as manifestation of correct operation, of cancelling the EPN, that reduces theoretically the noise to SN only, in which regime we expect a linear dependence with power, as shown by Eq. (1). For small optical powers, the noise for the balance configuration is slightly higher than the noise for the single camera configuration, due to the addition of two SN components, from the two cameras. As the power is increased, the noise for single camera increases faster, due to the EPN in Eq. (2) which varies with P^2, and exceeds the noise exhibited by the balance configuration.

#167225 - $15.00 USD Received 23 Apr 2012; revised 12 Jul 2012; accepted 13 Jul 2012; published 18 Jul 2012

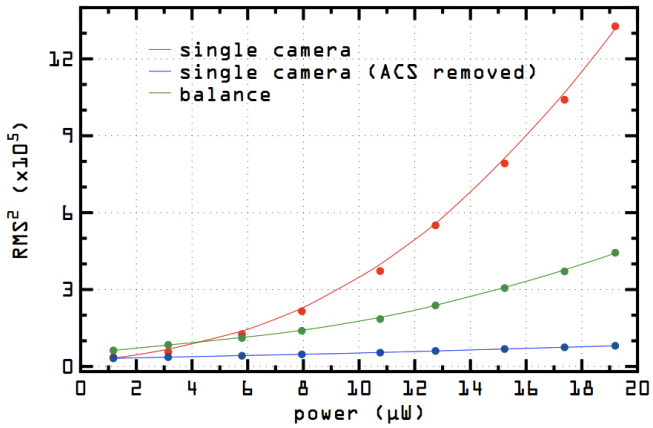

Fig. 12. RMS^2 vs. optical power measured at the input of one of the spectrometers. Red curve: single camera configuration; Blue curve: single camera configuration, ACS removed; Green curve: balance detection scheme.

However, if the ACS is deducted from the measurements of the single camera, a much improved result is obtained, as shown by the blue curve. A similar procedure employed to generate Figs. 9 and 10 was used, were averages of 512 FFT of spectra differences between the CS and ACS were performed. This procedure to reduce noise is largely used in the practice of FD-OCT. The only advantage for the balance detection is that the noise reduction shown by the green curve is obtained dynamically while due to power fluctuation of the optical source, the procedure of single camera with ACS deduction needs to be periodically updated.

In order to instigate more the effect of balance detection on the EPN, we produced A-scans using a large reference optical power, close to saturation. For the level of reference power used, the amplitude measured at each photo-detector site was typically superior to 8,000 counts. This corresponds to an optical power of 16.8 nW per photo-detector site, which by performing the inverse calculation with the factor of 0.86 and 512 pixels places the point of operation in the middle of the horizontal axis in Fig. 12, at ~10 μW, where the curve is already nonlinear. Consequently, at each photo-detector site, the EPN exceeds the shot noise. As an object, a mirror was used, tilted to return little power (~a few nW). In Fig. 13 bottom, we show the A-scans acquired for this reference power. For comparison, we also produced A-scans for a reference power reduced by a factor of 10, shown in the top row of Fig. 13. These correspond to a power where the graph in Fig. 12 is almost linear, i.e. where shot noise is dominant. A-scans are shown, for the two cameras used in single camera configuration (blue and red) and for the balance configuration (green). 512 A-scans were averaged to produce the graphs in Fig. 13. The data for the balanced configuration was obtained after correcting for non-identicalness of the two spectra, according to the procedure explained in connection with Fig. 2c. Apart from averaging 512 A-scans, no processing was applied for the data delivered by single cameras placed in the graphs in Fig. 13 left column. Balance detection in superior to the single camera configuration in both Fig. 13(a1) and Fig. 13(a2). The noise floor of the green graph is below the noise floor of the single camera configurations in Fig. 13(a1) and well below in Fig. 13 (a2). This is expected from the graph in Fig. 12 by comparing the red and the green curves.

In the right column, the graphs corresponding to single camera configurations were obtained after applying the deduction of ACS, similar to the procedure employed to generate Figs. 9 and 10. This leads to less noise floor for the single cameras in comparison with the balance detection configuration, as already shown by the green and blue graphs in Fig. 12. Using the insets in the right column, let us compare the increase in noise in each configuration

#167225 - $15.00 USD Received 23 Apr 2012; revised 12 Jul 2012; accepted 13 Jul 2012; published 18 Jul 2012

when increasing the reference power from 1 to 10 μW. As shown by the graphs in the two insets, the noise floor in the single camera configuration increases by an approximate factor of 1.4, while the noise floor in the balance configuration increases by a factor larger than 2. If the noise increase would have been due to EPN only, then we would have expected a larger increase in the noise in each single camera configuration than the increase in the balanced configuration. This shows that there might be other noise sources in the balanced configuration than the EPN and SN, or that there is EPN left after balance detection. This observation is in line with the deviation of the middle graph (green) in Fig. 12 for balance detection, from a linear behavior.

Comparing the ratio of noise between the balance detection and the single camera in the two reference power experiments leads to the same conclusion. Going from a single camera configuration to a balanced configuration, we expect for the noise to increase, due to the cumulative effect of two SN contributions, from the two cameras. If in the SN limited regime, the floor noise should have increased by $1.4 \cong \sqrt{2}$ times, which is the case in Fig. 13(b1) but larger than 2 in Fig. 13(b2), as a clear proof that there are other noise sources than shot noise.

There is no improvement in the signal-to-noise ratio by applying balance detection when compared with a single camera configuration equipped with deduction of ACS. At 1.6 mm, the signal almost doubles, from 500–600 to over 1200, while the noise increases by the same factor of 2.

Possible reasons for such behavior are:

- Synchronization issues. Although the two cameras are synchronized from a single signal generator, there is no way to ensure that each pair of photo-detector sites in the two arrays of 1024 (512 practically used), seeing the same wavelengths in the two spectrometers are read at exactly the same time, feature which can be secured with an array of photo-detectors only, that can be read in parallel, independently. For an acquisition time of 7 μs, optimum balance condition requires matching temporal events in ~7 ns for each photo-detector site (considering 1024 pixels);

- Alignment issues. The way in which the two spectrometers were aligned was based on overlapping the channeled spectra seen by the cameras. The alignment was performed for modulation frequencies as high as possible in the channeled spectrum, obtained for iteratively repeated measurements using different OPD values in the interferometer (creating anti-phase channeled modulation, hence maximum balance detection modulation) and with the glass plate halfway inserted into each of the beams (Talbot bands procedure [14]) giving in-phase channeled spectra modulation, hence cancelled modulation after balance detection. Despite this, some discrepancy in the alignment between the two modulated spectra could not be removed, especially by the spectrum edges;

- The quantum well capacity of the two cameras is still not sufficiently large to ensure a clear cut EPN contribution. Our measurement showed that the optical power at each photo-detector site was from 16.8 to 33.6 nW (on some pixels the optical power was lower than 16.8 nW), while theoretically we needed at least 16.4 nW at each photo site to be in the EPN regime. Pixels in the middle of the spectrum are close to saturation only, while the others are not, and pixels at the edges see much lower power levels. An ideal case to study the EPN would be to use a camera where a majority of pixels are illuminated by power over the threshold where EPN exceeds the SN;

- Differences between the two cameras that create uncorrelated noise during their reading.

#167225 - $15.00 USD Received 23 Apr 2012; revised 12 Jul 2012; accepted 13 Jul 2012; published 18 Jul 2012

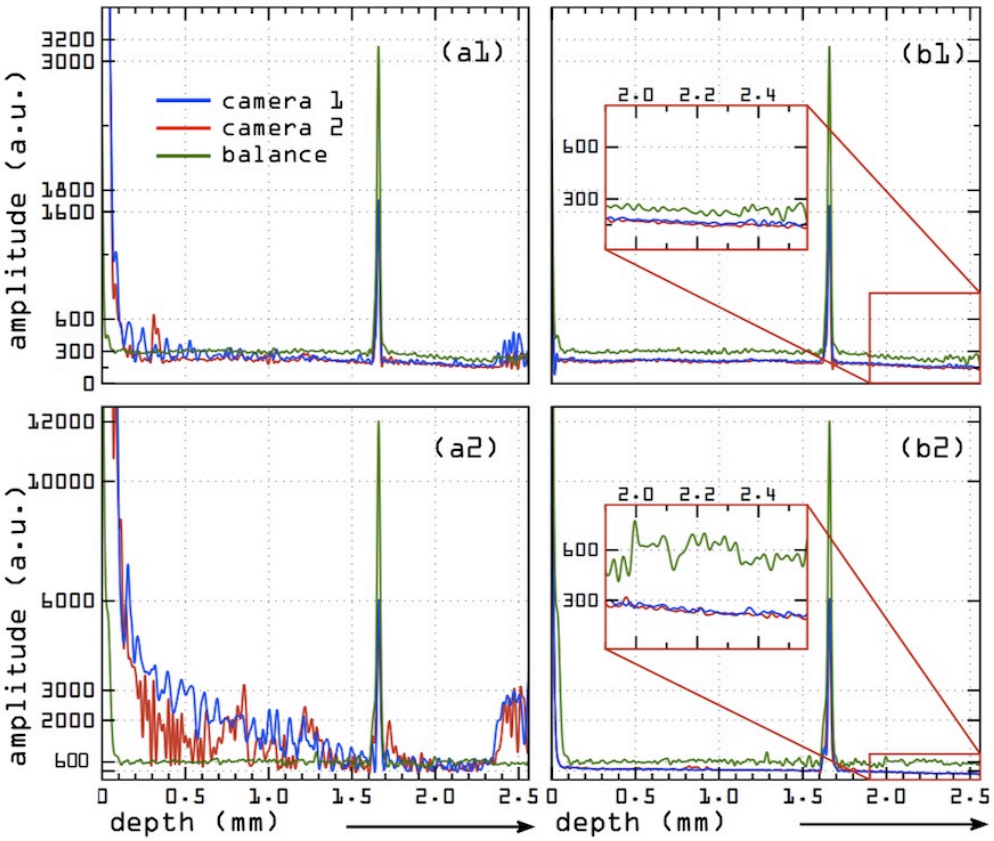

Fig. 13. Average of 512 A-scans from a flat mirror for two values of the reference power reaching each camera. Top row: reference power ~1 μW; Bottom row: reference power ~10 μW. In the right column, the graphs for the single camera configuration are obtained after ACS removal whilst the graphs for the balanced configuration after correction for the spectrum shape seen by each camera using the correction coefficient $C(\lambda)$ (see text).

4. Conclusion

In this paper we investigated the potential benefits that balance detection technique can bring to the enhancement of B-scan images produced by FD-OCT. We have evaluated the removal of artifacts and noise behavior. We demonstrated that a balance detection scheme can efficiently reduce autocorrelation terms. Balance detection eliminates the need of sequential procedures applied to single camera schemes, where several images or spectra are collected with one or both of the beams on and off. Such schemes would require deduction of images or averaged spectra from the currently measured image or spectrum respectively and are therefore sensitive to power variation. Therefore, balance detection scheme is more tolerant to variations of optical power in the process of removing the autocorrelation terms and of the fixed pattern noise artifacts. In addition, the balance detection technique operates in real time and therefore, is more tolerant to movements of the sample. Application of balance detection also eliminates the need of optical shutters to collect images or spectra with one of the beam on/off.

The optical power used and the quantum well value of cameras employed here, placed their regime of operation slightly higher than the threshold where the excess photon noise exceeded the shot noise. The balance detection proved capable of reducing the noise in comparison with a single camera configuration. However, deduction of averaged spectra from

#167225 - $15.00 USD Received 23 Apr 2012; revised 12 Jul 2012; accepted 13 Jul 2012; published 18 Jul 2012

the current spectra of single camera configuration reduced the noise even more. This simple procedure is largely used in the practice of FD-OCT and our comparative results demonstrate that a balance detection scheme may not be required for the task of reducing the EPN noise only. However, if progress in the technology of fast linear cameras continues, this may change and further work would be required with faster cameras of larger quantum well in order to fully evaluate the potential of reducing the noise in balance detection when applied to FD-OCT. Balance detection may however be the solution of choice when using unstable configurations, where power fluctuations may render the procedures based on deduction of averaged spectra as inefficient.

Acknowledgments

The authors acknowledge the support of the European Research Council grant 249889. The authors appreciate the help of Bayspec Inc. making a second InGaAs camera available as a loan and of Multiwave Photonics for lending us the optical source.

#167225 - $15.00 USD Received 23 Apr 2012; revised 12 Jul 2012; accepted 13 Jul 2012; published 18 Jul 2012